Title

Stabilizing Oxidative Dehydrogenation Active Sites at High Temperature with Steam: $ZnFe_2O_4$-Catalyzed Oxidative Dehydrogenation of 1-Butene to 1,3-Butadiene

Journal

ACS Catalysis, 10(21)

ISSN

2155-5435

Authors

Zeng, Tieqiang
Sun, Geng
Miao, Changxi
et al.

Publication Date

2020-11-06

DOI

10.1021/acscatal.0c03405

Stabilizing Oxidative Dehydrogenation Active Site at High Temperature with Steam: $ZnFe_2O_4$ Catalyzed Oxidative Dehydrogenation of 1-Butene to 1,3-Butadiene

Tieqiang Zeng,[†,‡] Geng Sun,[†] Changxi Miao,[‡] George Yan,[†] Yingchun Ye,[‡] Weimin Yang,*[,‡] and Philippe Sautet,*[,†,§]

[†]Department of Chemical and Biomolecular Engineering, University of California, Los Angeles, Los Angeles, California 90095, United States
[‡]State Key Laboratory of Green Chemical Engineering and Industrial Catalysis, Sinopec Shanghai Research Institute of Petrochemical Technology, Shanghai 201208, China
[§]Department of Chemistry and Biochemistry, University of California, Los Angeles, Los Angeles, California 90095, United States

ABSTRACT:
Dehydrogenation reactions are central for the production of functional molecules. Steam plays a pivotal role in $ZnFe_2O_4$ catalyzed 1-butene oxidative dehydrogenation (ODH). However, the essential effect of steam on this reaction is still unclear. Herein, we describe the structure-performance relationships of $ZnFe_2O_4$ in the presence/absence of steam by combined density function theory (DFT) and experimental studies. The catalytic performances of $ZnFe_2O_4$ under different reaction conditions were investigated. The $ZnFe_2O_4$(110) surface properties in reaction conditions and molecular reaction pathways were modeled. Free energy profiles were calculated. We found that an oxygen excess $ZnFe_2O_4$(110)-O termination, with an extra O atom bridging two Fe cations, is preferred under oxygen rich condition. However both experimental and theoretical approaches indicate that this surface bicoordinated O is not stable at relatively high temperatures in the absence of steam, resulting in reduction of surface Fe^{3+} cations to Fe^{2+} which are inactive in 1-butene ODH reaction. It was found that steam interacts strongly with the $ZnFe_2O_4$(110)-O surface. Steam stabilizes the catalyst surface Fe^{3+} ions by converting bicoordinated O to more thermally stable hydroxyl groups. Surface OH are active sites for C-H bond cleavage in 1-butene ODH reaction in the presence of steam. We propose that the role of steam elucidated here represents a general mode of steam influence in ODH reactions over oxide surfaces.

Keywords: Steam, zinc ferrite, oxidative dehydrogenation of 1-butene, 1,3-butadiene, DFT calculations, structure-activity relationship

INTRODUCTION

Oxidative dehydrogenation (ODH) of hydrocarbons is a very important reaction. Transition metal oxides are frequently used as efficient heterogeneous catalysts for ODH of hydrocarbons. However, the C-H bond is difficult to activate and significant barriers remains to be passed, which necessitates to operate at high temperature for high conversion. One problem is that the active site for H abstraction is surface O atoms, and these sites are not very stable at high

temperature where the metal tends to get reduced.[1-3] There is hence an incompatibility between the temperature requirements for activity and the stability of the active site.

ODH of butenes is a highly attractive process to produce 1,3-butadiene which is one of the most important bulk chemicals in the production of acrylonitrile-butadiene-styrene, butadiene rubber, styrene-butadiene rubber and plastics. Various catalysts have been investigated for the ODH of butenes, including ferrite-type catalyst,[4-9] Bi-Mo-based catalyst,[10-12] vanadium-based catalyst,[13,14] Pd-based catalysts,[15] Pt-based catalysts,[16] and carbon nanotube catalysts.[17] The nature of the active site for these ODH catalysts and the influence of reaction conditions are central questions in the domain. Among these catalysts, low-cost and environment-friendly metal ferrite compounds have been extensively studied as efficient catalysts for ODH of butenes and industrially applied since the 1970s. The spinel $ZnFe_2O_4$ is an active phase among these ferrite catalysts. Previous experimental studies shed some light on reaction and catalyst deactivation mechanisms for $ZnFe_2O_4$ catalyzed ODH of butenes.[18,19] However, to the best of our knowledge, no computational study has been performed to understand the reaction mechanism at the atomic-level.

Excess of steam is required in $ZnFe_2O_4$ catalyzed 1-butene ODH reaction to obtain a practical 1,3-butadiene yield, which is very energy consuming. Both activity and selectivity are significantly improved upon the introduction of steam to the reaction system, however the atomic-level understanding of the key role of steam is still missing. The hydroxylation of oxide catalyst surfaces has been intensively studied because steam is present in many industrial processes.[20-27] It is known to influence the acid-base properties and the activities in several catalytic systems.[25,28] Dissociative adsorption of water on $ZnFe_2O_4$ is also reported.[29,30] For example, Yang and co-workers suggested that the hydroxyls on metal ferrite catalysts modified by steam provide more basic sites and are more active than the corresponding hydroxyl-free oxide surfaces for 1-butene ODH reaction.[31] However, the question concerning which sites are more active for 1-butene ODH reaction is still open, and the reaction mechanism involving the steam addition remains elusive because of the missing atomic-level explanation.

In the present study, we unravel the critical role of steam in oxidative dehydrogenation of 1-butene on $ZnFe_2O_4$ catalyst. To achieve this objective, the nature of $ZnFe_2O_4$ surfaces were explored, and the catalytic properties of $ZnFe_2O_4$ under different reaction conditions, specifically at low/high temperature and in the presence/absence of steam, were investigated. The surface properties in reaction conditions and reaction pathways were modeled based on density functional theory (DFT), and the free energy profiles for reaction pathways were calculated. Comparing reaction pathways with and without co-fed steam, the essential role of steam was elucidated for the first time: stabilizing the active Fe^{3+} species.

EXPERIMENTAL AND COMPUTATIONAL METHODS

Catalyst Preparation and Characterization. 2.975 g $Zn(NO_3)_2 \cdot 6H_2O$ and 8.080 g $Fe(NO_3)_3 \cdot 9H_2O$ were mixed and dissolved in 200 mL absolute ethanol.[32] 0.62 g Ethanolamine was then added as the complexing agent, and the total solution was stirred for 4 hours at 60 °C. The resultant solution was then heated at 300 °C for 4 h in a muffle furnace to remove the solvent, and a further calcination was conducted at 650 °C for another 10 h to yield $ZnFe_2O_4$ catalyst. Its crystalline form was checked using powder X-ray diffraction. Then, the catalyst was imaged by high-angle annular dark field (HAADF) scanning transmission electron

microscopy (STEM) on a FEI Titan Cubed Themis G2 300 kV instrument with an accelerating voltage of 300 kV. X-ray photoelectron spectroscopy (XPS) was performed on a Thermo ESCALAB 250 spectrometer with a monochromatic $Al_{K\alpha}$ X-ray source (1486.6 eV) and an analyzer pass energy of 20 eV. The base pressure in the XPS chamber was kept under 10^{-9} Torr. The C 1s line at 284.6 eV was used to calibrate the binding energies (B.E.) of the elements. Fe 3p was used instead of the strongest photoemission line Fe 2p, due to core-hole relaxation effects in Fe 2p satellites lines. CO-FTIR spectra were recorded using a FTIR spectrometer (Bruker Vertex 70V) equipped with a stainless steel high vacuum transmission infrared cell. The calcinated $ZnFe_2O_4$ sample was pressed into spot on a tungsten mesh support. Prior to the experiment, the sample was cleaned under vacuum (2×10^{-8} mbar) at room temperature for 4 h. After cooling down to 130 K by using liquid nitrogen, the background spectrum was collected. Subsequently, 10 mbar of CO was introduced into the cell, and then the corresponding spectra were collected at indicated temperatures under 1×10^{-7} mbar. Then the sample was heated to 653 K under vacuum (1×10^{-7} mbar) overnight. After cooling down to 130 K, the background spectrum was collected. Then 10 mbar of CO was introduced into the cell, and the corresponding spectra were collected at indicated temperatures under 1×10^{-7} mbar.

1-Butene adsorption-desorption experiment was performed on the ChemBET/TPR/TPD unit (Quantachrome). Before adsorption, the catalyst pretreated by an O_2-steam mixture at 380 °C for 2 h was purged with helium at 200 °C for 2 h. 1-Butene was adsorbed on the catalyst at -78 °C. Excess gaseous 1-butene was removed by helium purging at -78 °C before stepwise thermal desorption of adsorbate. Helium gas passed through the catalyst at a flow rate of 30 mL/min at atmospheric pressure. The temperature was ramped with a rate of 0.5 K/s.

Catalytic Performance Test. The oxidative dehydrogenation of 1-butene was carried out using an isothermal fixed-bed downflow quartz reactor (10 mm i.d.) at 1 atm total pressure. First, 1.0 g $ZnFe_2O_4$ catalyst (particles of 0.1 - 0.2 mm) and 5.0 g quartz sand (particles of 0.1 - 0.2 mm) were placed upon a layer of inert glass wool. A thermocouple was used to monitor the temperature of the catalyst. Water was vaporized by passing through a pre-heating zone and continuously fed into the reactor together with 1-butene and air. The feed ratio of 1-butene: air: steam (or N_2 in the absence of steam) = 1: 3.8: 12. The GHSV (gas hourly space velocity) was 400 h^{-1} on the basis of 1-butene. Downstream from the reactor, steam was condensed and piped to a drain. The feed components and the reaction products were analyzed by an online gas chromatograph (Agilent 7890) equipped with PLOT/Q (for CO_2), activated Al_2O_3 (for hydrocarbons), and Molsieve 5 (for H_2, O_2, N_2, and CO) columns, flame ionization, and thermal conductivity detectors. The conversion of feed components, selectivity, and yield of the reaction products were calculated from the inlet and outlet concentrations considering the changes of reaction volume during the reaction. Reaction temperature was varied from 355 °C to 380 °C in the activation energy measurement while 30.4 mg catalyst was used and the 1-butene conversion was controlled below 15%.

DFT Calculations. DFT calculations were performed using the Vienna Ab-initio Simulation Package (VASP), version 5.4.1.[33,34] The projector augmented wave (PAW) method was used for modeling the interaction between valence electrons and effective cores.[35,36] The exchange-correlation energy was calculated using the Perdew-Burke-Erzenhof (PBE) functional,[37] and the dDsC correction was exploited for van der Waals (vdW) interaction.[38] A cutoff energy of plane-wave of 520 eV provides converged electronic energies. A Hubbard U of U_{eff} = 5.3 eV

is also applied to the Fe d orbitals to describe strong correlation effects. With this value, the DFT calculated redox properties during lithiation and computed lattice parameter and magnetic moment for $ZnFe_2O_4$ agree well with the experimental values.[39,40] A symmetric 7-layer $ZnFe_2O_4$(110) slab, corresponding to a (1x2) supercell was used for the calculations. The atoms (1 layer) in the center of the slab are fixed at their bulk positions while the other atoms are allowed to fully relax. The Brillouin zone is sampled using a 4 × 3 × 1 Monkhorst-Pack mesh. Atomic positions are relaxed until forces on unconstrained atoms fall below 0.02 eV/Å during structure optimization. A vacuum of 20 Å is introduced in the Z-direction to avoid the interaction between the periodic images, and the dipole correction is also applied.
The surface energy of each termination is calculated according to:

$$\gamma = \frac{1}{2A}\left(E_{slab} - \Sigma N_i \mu_i\right) \qquad (1)$$

where E_{slab} is the electronic energy of the clean (1x2) $ZnFe_2O_4$(110) slab of chosen termination. N_i and μ_i are the number of atoms of type i in the slab and its chemical potential, respectively. A is the surface area of the slab. The factor 2 arises from the existence of two identical surfaces. Surfaces with water adsorption are compared by relative surface free energies, defined as:

$$\Delta\gamma_{slab+nH_2O} = (G_{slab+nH_2O} - G_{slab} - n \cdot G_{H_2O})/A \qquad (2)$$

Where G_{slab}, $G_{slab+nH_2O}$ and G_{H_2O} are the Gibbs free energy of the bare slab, slab with n adsorbed H_2O molecules, and a single gas phase H_2O molecule respectively. The enthalpy of slab was approximated as the sum of the electronic energy and the zero-point energy using harmonic frequencies. Vibrational frequencies are calculated using finite differences with a displacement of 0.015 Å. The changes in the Fe oxidation state can be identified by magnetic moments, i.e. 3.65-3.78 μB for Fe^{2+} and 4.20-4.36 μB for Fe^{3+}.[41] Gibbs free energies of gas phase water were calculated using standard formulas for rotational, translational, and vibrational freedoms.[42] When calculating the adsorption free energies of water on the $ZnFe_2O_4$ surfaces, electronic energy and the zero-point energy of condensed phases were accounted. Transition state structures are located by the NEB method.[43,44] A vibrational analysis was conducted on the optimized transition states, confirming that only one imaginary frequency is present.

RESULTS AND DISCUSSION

$ZnFe_2O_4$ Surfaces: Structures and Stability

In a 56-atom $ZnFe_2O_4$ cubic supercell constructed from the 14-atoms primitive cell, the DFT optimized lattice parameter of 8.504 Å (8.52 Å in experiment)[45] and magnetic moment of 4.3 μB (4.2 μB in experiment)[46] agree well with the experimental values. An antiferromagnetic spin arrangement (Figure S1) was found to correspond to the lowest energy, which is in consistent with reported results.[47,48] The synthesized $ZnFe_2O_4$ catalyst was imaged via scanning tunneling electron microscopy (STEM).[49,50] The HAADF-STEM image (Figure 1) revealed that in perpendicular sections the two in plane directions are $[1\bar{1}0]$ and [001], which indicates that the sample was inspected from the [110] direction. The STEM result also shows that the (110) surface is preferentially exposed in this $ZnFe_2O_4$ catalyst.

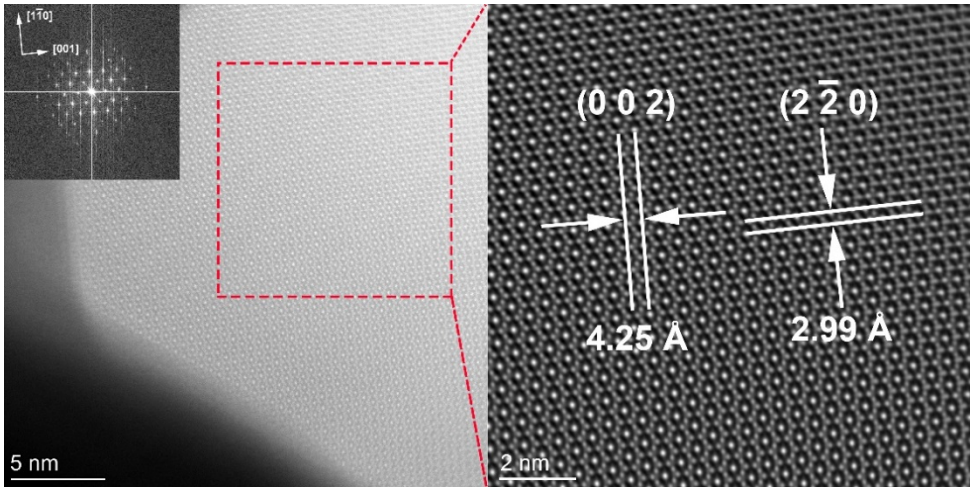

Figure 1. HAADF-STEM image of $ZnFe_2O_4$ sample marked with lattice fringes and corresponding Fast Fourier transformation (FFT) patterns (inset).

Based on the STEM images, we chose a 7-layer (1x2) (110) surface to model the $ZnFe_2O_4$ catalyst, in which the antiferromagnetic spin arrangement was optimized (Figure S2). Along the [110] direction, the atoms are stacked by the repeated sequence of [-$Zn_4Fe_4O_8$-Fe_4O_8-]. A 7 layer slab insures a sufficient convergence of the energy with thickness. To explore the stability of surfaces under O-poor to O-rich conditions, various terminations including Fe_4O_7, Fe_4O_8, $Zn_4Fe_4O_8$, O and O_2 were considered (Figure 2 and Figure S3). Each termination is indicated by its composition. In the case of the O termination, the outermost layer is composed of one oxygen atom which bonds to two Fe atoms in the second layer composed of $Zn_4Fe_4O_8$. The Fe-O bond lengths are 1.82 Å. The outermost layer of (110)-O_2 surface is composed of two oxygen atoms. This represents a significant excess of O on the surface (coverage of 2 O for 1.02 nm^2 of surface, i.e. for 4 surface Fe). Higher O coverage situations such as (110)-O_3 and (110)-O_4 were calculated to be less stable than the (110)-O and (110)-O_2 surfaces at $\Delta\mu_O < 0$ (stability diagram see Figure S4). The O poor Fe_4O_7 termination is obtained by removing an oxygen atom which is surrounded by three Fe atoms from the Fe_4O_8 termination. Chemical potentials of Zn, Fe, and O atoms are limited by constraints to maintain the bulk stability. $\Delta\mu_{Zn}$, $\Delta\mu_{Fe}$, and $\Delta\mu_O$ are constrained by the formation enthalpy of bulk $ZnFe_2O_4$ (see S1). To avoid the metal precipitation, lattice oxygen releasing into the environment, or the formation of binary oxides (i.e. Fe_2O_3 or ZnO), $\Delta\mu_{Zn}$, $\Delta\mu_{Fe}$, and $\Delta\mu_O$ should also satisfy the conditions listed in S1. Based on DFT calculated surface energies, only the (110)-$Zn_4Fe_4O_8$, (110)-O, and (110)-O_2 surfaces were found to be stable under the range of chemical potentials where $ZnFe_2O_4$ bulk is stable (Figure 2). Specifically, the (110)-O_2 surface is stable when $\Delta\mu_O > -0.08$ eV (at low temperature and high O_2 pressure). The (110)-O surface is preferred under oxygen rich condition, and the (110)-$Zn_4Fe_4O_8$ surface is more stable under oxygen poor condition. The phase transition between the (110)-O surface and the (110)-$Zn_4Fe_4O_8$ surface takes place at $\Delta\mu_O = -0.72$ eV. Under reaction conditions in the absence of steam (Figure 3), $\Delta\mu_O \leq -0.76$ eV and therefore we can expect that the (110)-O surface tends to lose the outermost bicoordinated O^{2-} and transform to the (110)-$Zn_4Fe_4O_8$ surface.

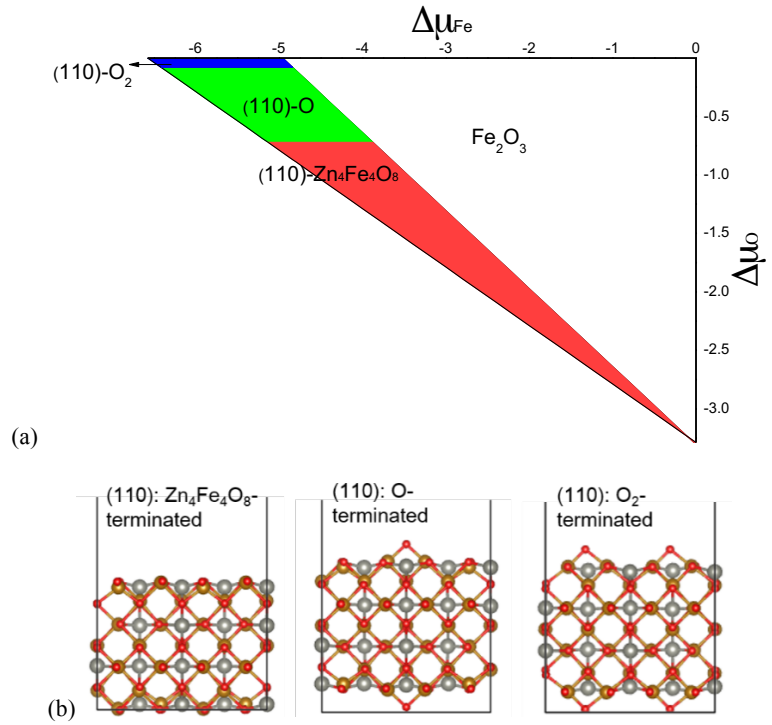

Figure 2. (a) Surface stability diagram as a function of O and Fe chemical potentials and (b) corresponding structures of stable terminations for the $ZnFe_2O_4$(110) surface (iron atoms shown as golden balls, zinc atoms as silver balls, oxygen atoms as red balls). The colored region in (a) corresponds to the stability zone of bulk $ZnFe_2O_4$.

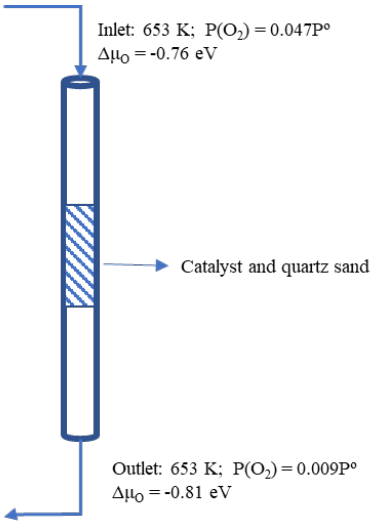

Figure 3. Evaluation of $\Delta\mu_O$ for reactor inlet and outlet over $ZnFe_2O_4$ catalyzed 1-butene ODH. Reaction conditions: 1.0 g catalyst, 653 K, 0.1 MPa, 1-butene: air: N_2 = 1: 3.8: 12, 1-butene GHSV = 400 h^{-1}.

All iron atoms in the (110)-O slab are Fe^{3+} (formula $Zn_{16}Fe(III)_{28}O_{58}$), while as the (110)-O surface loses the outermost O atoms, four Fe^{3+} (two on each surfaces) will be reduced to surface Fe^{2+} resulting in the formula $Zn_{16}Fe(III)_{24}Fe(II)_4O_{56}$. XPS was used to characterize the oxidation state of Fe on $ZnFe_2O_4$ surface. The fitted peak at 54.5 eV (Fe 3p) is ascribed to Fe^{2+} ions.[51] The XPS observations confirm that no obvious Fe^{2+} is present in the as-prepared $ZnFe_2O_4$

catalyst, demonstrating that the outermost O atoms are stable under room temperature and high vacuum (1× 10^{-9} Torr, test chamber pressure). However, a peak representing Fe^{2+} species (Fe^{2+}/Fe^{3+} = 0.3) was clearly observed for the $ZnFe_2O_4$ sample which was treated at 653 K for 2 h under vacuum (Figure 4b), indicating partial reduction of the surface. Considering that the attenuation lengths are about 1-10 monolayers for the emission angles normal to the surface,[52] and only half amount of surface Fe^{3+} is expected to be reduced to surface Fe^{2+} at 653 K, the XPS results are in line with theoretical analysis. FTIR using CO as a probe molecule was also applied to identify the surface properties of $ZnFe_2O_4$ by measuring the vibrational frequency of adsorbed CO.[3,53] The frequency and intensity of the CO stretch vibration is extremely sensitive to the oxidation state and electronic environments of surface Fe cations. As shown in Figure 5, only the Fe^{3+}-related CO vibrations at 2152 and 2103 cm^{-1} were observed for the as-prepared $ZnFe_2O_4$ surface. In comparison, new intense Fe^{2+}-related CO bands at 2210, 2109, 2098, 2074 and 2064 cm^{-1} were detected for the sample which was treated at 653 K under vacuum, meanwhile characteristic band at 2152 cm^{-1} for Fe^{3+} site was also observed. The stronger binding of CO to Fe^{2+} can be attributed to the enhanced electron back-donation to the CO $2\pi*$ antibonding orbital. Interestingly, it seems that the Fe^{2+}-related CO band positions are sensitive to the desorption temperature and shift from 2109 and 2098 cm^{-1} observed at 223 K to 2074 and 2064 cm^{-1} observed at 233 K, which possibly caused by the configuration change of the absorbed CO.[54] The results of both the XPS and FTIR analyses confirmed that a fraction of surface Fe^{3+} will be reduced to Fe^{2+} at 653 K, indicating that the outermost O atoms are unstable at high temperature. The reduced $ZnFe_2O_4$ surface was found to be inactive in 1-butene ODH reaction by us and others.[7,55] The conversion of 1-butene decreased to near 0% when active surface oxygen were consumed (Figure S5).

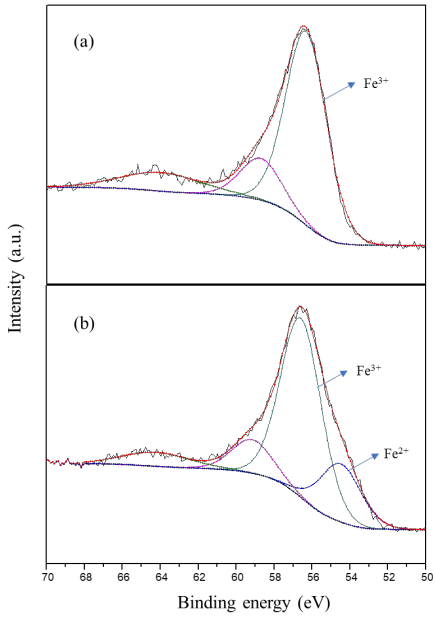

Figure 4. The XPS spectrum of Fe 3p from the surface of (a) as-prepared $ZnFe_2O_4$, and (b) $ZnFe_2O_4$ which was kept at 653 K and ~10^{-4} Torr vacuum for 2 hours and then cooled down to room temperature under 10^{-7}-10^{-8} Torr vacuum.

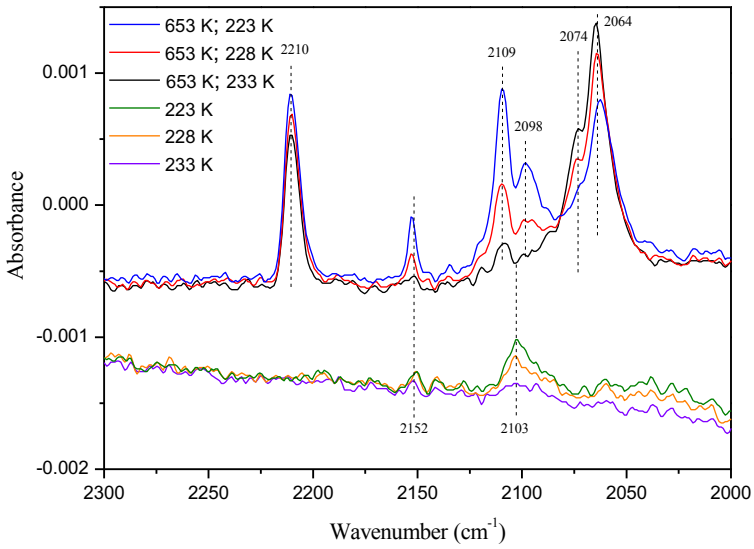

Figure 5. FTIR spectra of CO adsorbed on as-prepared $ZnFe_2O_4$ and $ZnFe_2O_4$ which was kept at 653 K under vacuum (1×10^{-7} mbar) overnight. 653 K indicates that the sample was treated at 653 K in UHV prior to CO adsorption. Spectra were recorded at indicated temperatures (223, 228 or 233 K).

Dissociative Water Adsorptions on the $ZnFe_2O_4$(110) Surfaces

Water adsorption on $ZnFe_2O_4$ was investigated by Tabari et al,[30] and they suggest that the initial water adsorption was dissociative adsorption. To gain a deep understanding of the interaction between H_2O and the $ZnFe_2O_4$ surface, DFT calculations were performed to study the adsorption sites of H_2O on the $ZnFe_2O_4$(110)-O and (110)-$Zn_4Fe_4O_8$ surface terminations in this paper. H_2O adsorption is considered on one side of the exposed surfaces of the slab. For each H_2O molecule adsorbed, both molecular and dissociative adsorptions are computed. The results showed that the first five H_2O molecule adsorptions on the (110)-O surface and the first three H_2O molecule adsorptions on the (110)-$Zn_4Fe_4O_8$ surface are dissociative adsorptions (structures are shown in Table S1). This corresponds to a maximum OH coverage of 9.8 and 5.9 per nm^2, on (110)-O and (110)-$Zn_4Fe_4O_8$ respectively. Further H_2O adsorptions are not considered here because they are not stable on the surfaces under elevated temperature. Each H_2O dissociation leads to two hydroxyls on the surface. Regarding the origin of OH, we denote surface derived hydroxyl as O_sH and water-derived hydroxyl as O_wH.

On the (110)-O surface, each oxygen atom of O_wH derived from the first to the third H_2O molecule bonds to two Fe atoms in the $Zn_4Fe_4O_8$ layer, on a bridge site, and the Fe-O bond lengths are in the range of 1.99-2.03 Å. Each oxygen atom of O_wH derived from the fourth and the fifth H_2O molecule bonds to a Zn atom in the $Zn_4Fe_4O_8$ layer, and Zn-O bond lengths are in the range of 2.00-2.02 Å. For the first H_2O molecule adsorption, the dissociated H binds to the outermost bicoordinated O atom forming an O_sH group. The H atoms dissociated from the second to the fifth H_2O molecule move to the adjacent O atoms in the $Zn_4Fe_4O_8$ layer. The stepwise adsorption energy of one to five H_2O molecules is -2.33, -1.24, -1.13, -0.99 and -0.75 eV, respectively. The surface energies revealed that five H_2O adsorption is preferred at low temperature (400K, 1 bar), while one H_2O adsorption is the most stable situation under 1-butene ODH reaction temperature (Figure 6).

On the (110)-$Zn_4Fe_4O_8$ surface, each oxygen atom of O_wH derived from the first to the third

H_2O molecule bonds to two Fe atoms in the $Zn_4Fe_4O_8$ layer, and the Fe-O bond lengths are in the range of 2.00-2.08 Å. The H atoms from H_2O molecules move to the adjacent O atoms in the $Zn_4Fe_4O_8$ layer. The stepwise adsorption energy of one to three H_2O molecules is -0.80, -1.14, and -0.88 eV respectively. Hence the (110)-$Zn_4Fe_4O_8$ surface is not hydroxylated under 1-butene ODH reaction conditions (Figure S6).

To identify the nature of the catalyst surface under reaction conditions (653 K, O_2: 0.047 P^o, H_2O: 0.71 P^o), we further determined the most stable termination of the surface in the presence of a water pressure, by comparing surface energies for the (110)-O and (110)-$Zn_4Fe_4O_8$ terminations with a variable number of water molecules chemisorbed, and fixing $P(O_2)$ = 0.047 P°. As depicted in Figure 6, at high temperature, the (110)-O surface tends to lose the outermost O atom at low water pressure, forming (110)-$Zn_4Fe_4O_8$ with partial Fe reduction, while at higher water pressure, the hydroxylated (110)-O termination is the most stable one (structure (110)-O-1H_2O). Therefore, this surface oxygen is stabilized by H_2O dissociative adsorption, highlighting the critical role of H_2O in stabilizing Fe^{3+} under reaction conditions. The surface stability as a function of temperature and oxygen pressure is shown in Figure S7 (fixing $P(H_2O)$ = 0.71 P°). The surface stability is not sensitive to $P(O_2)$ at low temperature, while at higher temperature (>700 K), a high-pressure of O_2 stabilizes the hydroxylated $ZnFe_2O_4$(110)-O-1H_2O termination.

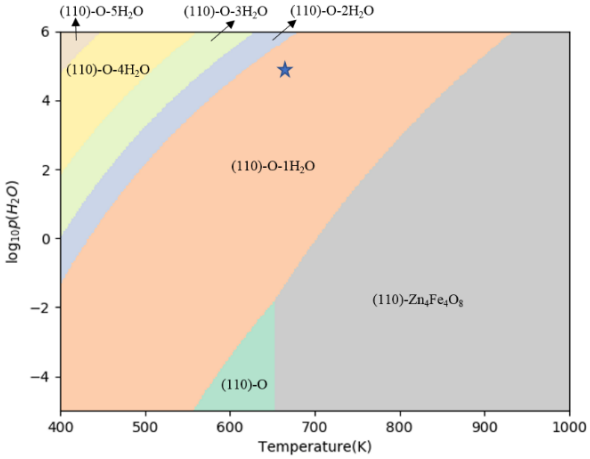

(a)

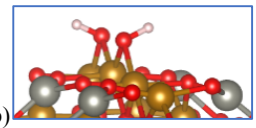

(b)

Figure 6. (a) Stability diagram for the surface as a function of temperature and water pressure, considering the (110)-O and (110)-$Zn_4Fe_4O_8$ terminations with a variable number of water molecules. The most stable termination is indicated in the diagram as a function of conditions. The equilibrium is here constrained, fixing $P(O_2)$ = 0.047 P°. The star represents the 1-butene ODH reaction conditions, 653 K and $P(H_2O)$ = 0.71 P^o; (b) structure of the (110)-O-1H_2O surface.

$ZnFe_2O_4$ Catalyzed 1-Butene ODH: Influence of Steam

The effect of steam on the performance of the $ZnFe_2O_4$ catalyst (surface area: 18.4 m^2/g) is given in Figure 7. For example, at O_2: 1-butene = 0.8 (mol: mol), the introduction of steam markedly increased the conversion from 38% to 80%, and raised the selectivity from 75% to 94%, in which the main byproducts are CO_2 and CO.

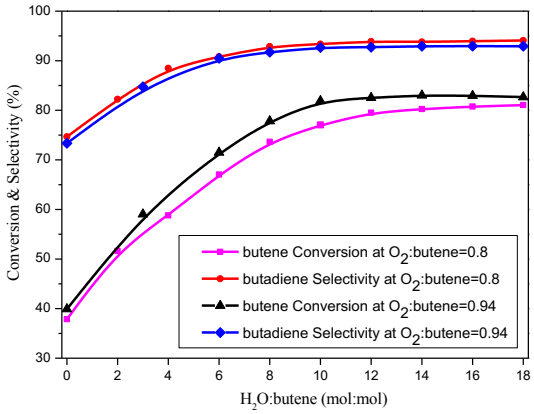

Figure 7. Catalytic performance as a function of H_2O: 1-butene ratio over $ZnFe_2O_4$. Reaction conditions: 1.0 g catalyst, 653 K, 0.1 MPa, 1-butene: air = 1: 3.8 (or 4.465), 1-butene GHSV = 400 h^{-1}.

Figure 8 shows the changes of conversion and selectivity for butadiene with increasing reaction temperature over $ZnFe_2O_4$ in the presence of steam (based on single catalyst loading, without regeneration requirement). It can be seen that almost 100% of butadiene selectivities were obtained at low 1-butene conversions (< 0.2%) and low temperatures (403-473 K, the 1-butene conversion was 0.03% at 403 K). The CO_x selectivity increased to 6% when temperature was raised to 483 K, meanwhile the 1-butene conversion was still very low (0.4%). A substantial increase in conversion and a slight change in butadiene selectivity were observed when temperature was increased from 483 K to 653 K.

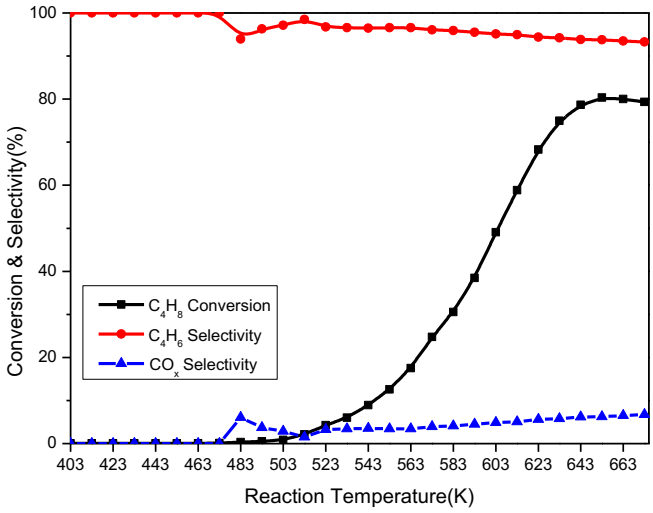

Figure 8. Catalytic performance as a function of reaction temperature over $ZnFe_2O_4$ in the presence of steam. Reaction conditions: 1.0 g catalyst, 0.1 MPa, 1-butene: air: steam = 1: 3.8: 12, 1-butene GHSV = 400 h^{-1}.

In order to validate the DFT calculations and the proposed surface models, we also examined the physical adsorption of 1-butene on the catalyst pretreated by an O_2-steam mixture at 653 K. After equilibrating the surface with 1-butene molecules, a stepwise thermal desorption was performed to monitor the desorption as a function of temperature. The results are given in Figure S8, which shows the amounts of 1-butene desorption at each temperature. It should be noted that butadiene was detected in the desorption C4 flow (6-12 vol % at 300-400 K),

indicating the surface is already active for ODH at these temperatures. DFT calculations for 1-butene adsorption on the (110)-O-1H_2O surface show that the C=C bond in 1-butene is adsorbed at the Zn atom with an adsorption energy of -0.93 eV. The adsorption Gibbs free energies have been calculated (at P(1-butene) = 10 Pa, measured by GC), and ΔG_{ads} is negative at 300 K and become positive at 400 K (Figure S8). The change of sign of ΔG_{ads} agrees very well with experimental results. Assuming a first-order desorption process with a constant pre-factor, the activation energy of desorption for 1-butene on the (110)-O-1H_2O surface is calculated to be 0.99 eV applying the Redhead equation:[56]

$E/RT_p = \ln(\upsilon T_p/\beta) - 3.64$ (3)

where R is the Boltzmann constant, υ is the frequency factor (10^{13} s^{-1}), T_p is the desorption peak maximum (350 K), and β is the heating rate (0.5 K/s). This result agrees with the DFT calculation which gives a desorption energy of 0.93 eV (Figure S10).

$ZnFe_2O_4$ Catalyzed 1-Butene ODH: Reaction Pathways

DFT calculations were performed to investigate the 1-butene ODH reaction mechanism. In order to highlight the effect of steam, we calculated and compared reaction pathways on a bare (110)-O surface and on hydroxyl pre-covered surface. In addition, the possible initial step of deep oxidation to form CO_x was investigated to understand the selectivity.

The calculated Gibbs free energy profiles at 650 K for 1-butene ODH on the (110)-O-1H_2O surface are shown in Figure 9 (assuming a 1-butene conversion of 5%, O_2: 0.045 P^o, H_2O: 0.72 P^o, 1-butene: 0.057 P^o, butadiene: 0.003 P^o; corresponding structures are shown in Figure 9 and Figure S9). The first C-H bond breaking occurs at the allylic position.[57] The allylic hydrogen atom is abstracted by a Fe-OH-Fe hydroxyl site to form an adsorbed molecular water through a transition state TS1 (the spin density of TS1 is shown in Figure S11). A surface Fe^{3+} ion is reduced to Fe^{2+} in this process as seen with its magnetic moments.[41] The energy barrier of the first H rupture is 1.17 eV. Subsequently, the terminal carbon (by resonance effect) of the resulting C_4H_7 group binds to a surface oxygen site (IM1). After the desorption of water, the second H is abstracted by another hydroxyl group to form adsorbed water and butadiene molecules, accompanied by the reduction of another Fe^{3+} ion in the -Fe-OH structure. After the desorption of water and of the butadiene molecule, two surface Fe^{2+} are re-oxidized by gaseous O_2 to form a superoxide (-Fe-O-O-Fe-) structure. Two successive H ruptures in another 1-butene molecule produce the second butadiene. The first C-H activation to form a C_4H_7* and a surface hydroperoxide structure is activated by a superoxide site with an energy barrier of 0.34 eV, which is lower than the energy barriers of H ruptures by the Fe-OH-Fe sites. The second H rupture on the newly generated hydroperoxide produces butadiene and water, which subsequently dissociatively adsorbs on the catalyst surface. The superoxide structure is predicted to be not thermodynamically stable at high temperature, and we speculate that this is the reason for the gradual decrease of catalytic activity as reaction temperature is increased above 653 K (Figure 8). The calculated results illustrated that the rate determining step in the reaction is the first C-H activation step, and the reaction barrier is 1.17 eV. The experimental measured apparent activation energy is 1.43 eV (Figure 10), which confirms the experimental necessity for high operating temperatures.

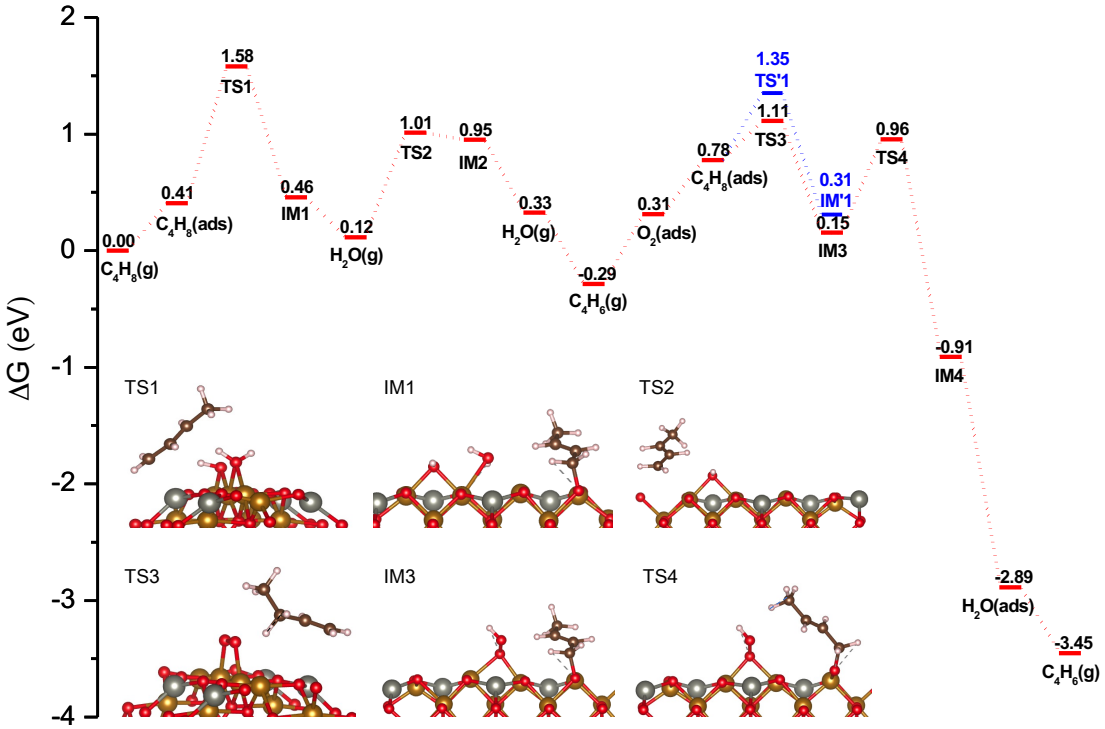

Figure 9. Calculated free energy profiles of 1-butene ODH on the (110)-O-1H_2O surface (650 K). Profile starts from 1-butene (gas) as zero reference. The red color illustrates the butadiene channel, and the blue color illustrates the initial step of CO_x channel. g stands for gas phase species and ads stands for adsorbed species. All the energies are in eV. The key structures of transition states and intermediates have been shown in the diagram (iron atoms shown as golden balls, zinc atoms as silver balls, oxygen atoms as red balls, carbon atoms as brown balls, hydrogen atoms as white balls).

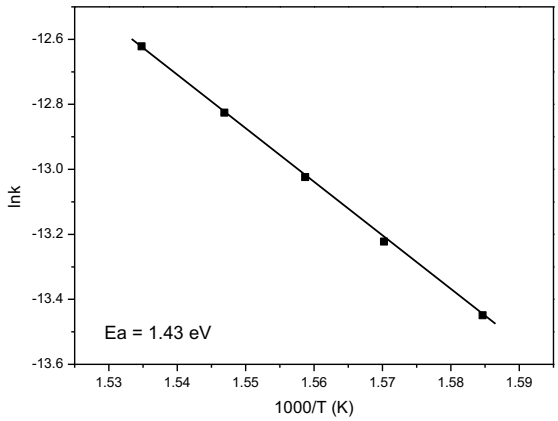

Figure 10. Arrhenius plots of 1-butene ODH rates over $ZnFe_2O_4$. 30.4 mg catalyst, 1-butene GHSV = 46667 h^{-1}, 1-butene: air: steam = 1: 3.8: 12.

Pure butadiene gave 0.2-0.3% conversion and almost 100% selectivity to CO_x when it was used as reactant (1.0 g catalyst, 0.1 MPa, 653 K, butadiene: air: steam = 1: 3.8: 12, butadiene GHSV = 400 h^{-1}), demonstrating that CO_x was mainly produced by the deep oxidation of 1-butene in 1-butene ODH. The adsorbed 1-hydroperoxybut-2-ene (IM'1, more stable than the adsorbed 3-hydroperoxybut-1-ene isomer), a possible intermediate of CO_x formation, can be generated via: (1) the reaction of 1-butene with superoxide in which the C_4H_7 group binds to an oxygen in -

Fe-O-O-Fe- site (Figure 11), and (2) the migration of C_4H_7* in IM3 to an oxygen in -OOH site with an energy barrier of 1.25 eV (transition state structure see Figure S12). The calculated results show that the pathway for butadiene is more competitive. Therefore, butadiene is obtained as main product but the formation of 1-hydroperoxybut-2-ene appears as a selectivity limiting side reaction.

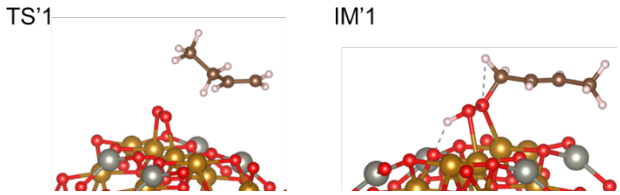

Figure 11. The structures of intermediate and transition state structures for the initial step to form CO_x.

Higher O_2: 1-butene ratio is expected to increase the coverage of superoxide site, keep the surface oxidized and facilitate the formation of surface OH group (Figure S7). Therefore, as shown in Figure 7, a small increase in O_2: 1-butene ratio (from 0.8 to 0.94) increased the conversion, and slightly reduced the steam requirement and the butadiene selectivity.

As shown in Figure 12, in the absence of steam, the butadiene selectivities were near 100% at relatively low temperatures (403-483 K, the 1-butene conversion was 0.2% at 403 K), and decreased to 70-80% when the temperature was above 493 K. The maximum 1-butene conversion was obtained at 623 K.

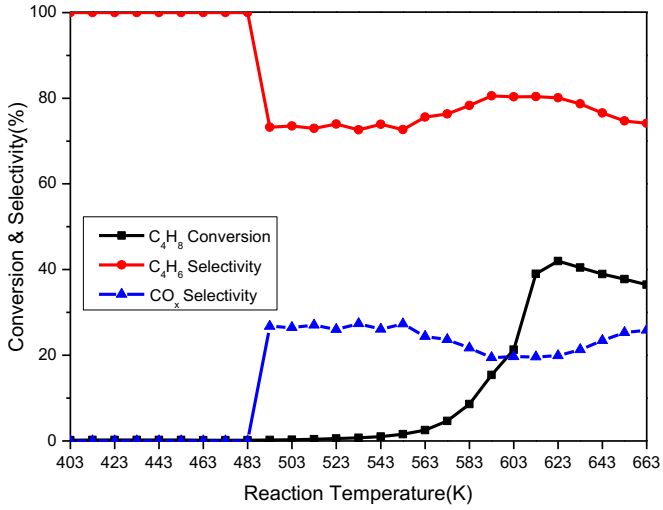

Figure 12. Catalytic performance as a function of reaction temperature over $ZnFe_2O_4$ in the absence of steam. Reaction conditions: 1.0 g catalyst, 653 K, 0.1 MPa, 1-butene: air: N_2 = 1: 3.8: 12, 1-butene GHSV = 400 h^{-1}.

We conducted 1-butene ODH calculations on (110)-O surface to study the reaction mechanism in the absence of steam (assuming a 1-butene conversion of 5%, 1-butene: 0.057 P^o, O_2: 0.045 P^o, H_2O: 0.003 P^o, butadiene: 0.003 P^o, Figure 13). On the (110)-O surface, the first hydrogen atom is abstracted by the bicoordinated O to form a hydroxyl group with an energy barrier of 0.25 eV. The second H is abstracted by the newly generated hydroxyl group to form water and butadiene molecules, the high activation barrier results from the strong adsorption of C_4H_7* on the surface oxygen. The subsequent re-oxidation of surface Fe^{2+} and C-H activation steps are

in the same with the processes on the (110)-O-1H_2O surface. The effective free energy barrier (energetic span[58]) is controlled by the second part of the reaction and the formation and reaction steps on the surface superoxide. It amounts to 1.4 eV, which is slightly lower than the effective free energy barrier on the (110)-O-1H_2O surface (1.58 eV). However, as mentioned above, only a low coverage of bicoordinated O is expected to exist on the surface because of its low stability at high reaction temperature, resulting in a relatively low 1-butene conversion. It is speculated that the coverage of bicoordinated O would reach a dynamic equilibrium on the surface when a steady flow of O_2 is introduced into the 1-butene ODH reaction. Therefore, the catalytic performance of $ZnFe_2O_4$ in 1-butene ODH reaction in the absence of steam is stable under 653 K and 0.1 MPa (Figure 13).

There is no obvious CO_x formation in the absence of gaseous O_2 (Figure S5). The reaction begins to produce CO_x at similar temperatures (483-493 K) under both reaction conditions with or without steam. These results suggest that CO_x is formed following the same mechanism on the (110)-O and (110)-O-1H_2O surfaces. The superoxide structure acts as active site for deep oxidation. As mentioned above, the binding of C_4H_7* to the -O-O- site yields a possible intermediate of deep oxidation. However, as we can see, more CO_x was formed on the (110)-O surface. This can be explained by the concentrations of the C_4H_7* intermediates on the considered surfaces. On the (110)-O-1H_2O surface, the first C-H activation of the first 1-butene is the rate determining step. The second H rupture of the first 1-butene is faster than the first H abstraction which generate C_4H_7* on the surface (IM1, Figure 9). Therefore, a low concentration of C_4H_7* is expected to remain on the surface. On the other hand, on the (110)-O surface, the second H rupture of the first 1-butene is slower than the first H abstraction, resulting in a higher concentration of C_4H_7* intermediates on the surface, and hence a higher probability to react with superoxide spices to form CO_x.

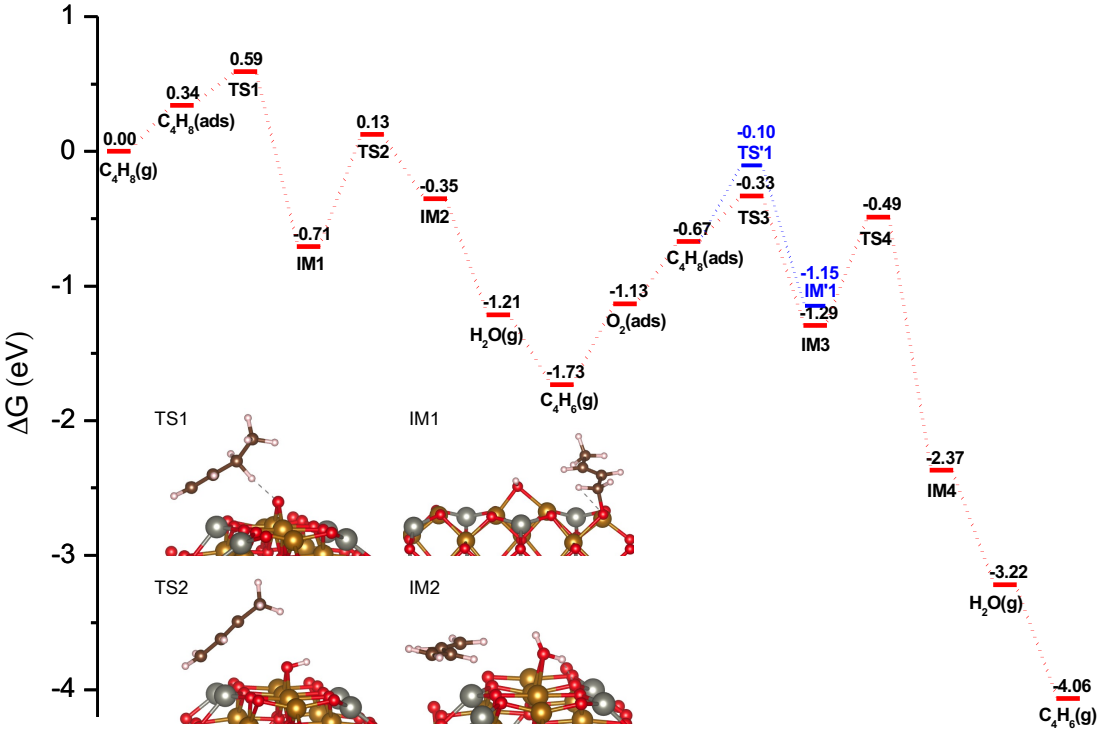

Figure 13. Calculated free energy profiles of 1-butene ODH on the (110)-O surface (650 K). Profile starts from 1-butene (gas) as zero reference. The red color illustrates the butadiene channel, and the blue

color illustrates the initial step of CO_x channel. g stands for gas phase species and ads stands for adsorbed species. All the energies are in eV. The key structures of transition states and intermediates have been shown in the diagram.

The simulation results depicted in Figure 6 also indicate that at 900 K, H_2O tends to desorb from the (110)-O-1H_2O surface at high water pressure ($P(H_2O) = 0.71\ P^o$), implying that steam will not play a significant role in 1-butene ODH reaction in such conditions. The results agree with experiments where only a slight promotion effect of steam was observed: the 1-butene conversion was increased from 38% to 46%, and the butadiene selectivity was increased from 66% to 74% at 900 K.

CONCLUSION

In this work, a combination of experimental results and DFT analyses over $ZnFe_2O_4$ catalyzed 1-butene ODH reactions revealed the key role of steam on the stabilization of the active O species at high temperature and on the catalytic activity. The $ZnFe_2O_4$(110)-O surface tends to lose the bicoordinated oxygen (Fe-O-Fe) at high reaction temperatures, resulting in reduction of Fe^{3+} ions in the surface which was confirmed by both XPS and CO-FTIR analyses, and loss of activity. H_2O interacts strongly with the $ZnFe_2O_4$(110)-O surface, leading to the formation of hydroxyl groups, a structure which is thermodynamically stable at reaction temperature of 1-butene ODH. 1-Butene ODH reactions on the $ZnFe_2O_4$(110)-O and $ZnFe_2O_4$(110)-O-1H_2O surfaces were systematically investigated using both experimental and theoretical approaches to establish the structure-activity relationships. The good agreement between 1-butene adsorption energy on the site and the measured value from 1-butene TPD validates the structure of the site obtained by calculations on the (110) surface. The surface OH groups and the surface O species are both active sites for C-H bond breakage, and their regeneration goes through the formation of a surface superoxide species, that is active for both butene dehydrogenation and deep oxidation, restoring the initial site. However, the surface O species is not stable at the high temperature required to obtain a reasonable rate for the reaction. This explains the low activity in dehydrated conditions. In the presence of steam, the double hydroxyl structure formed by chemisorption of one water molecule on each surface O species is calculated by first principle thermodynamics to be stable until 900 K at a water pressure of 0.71 P^o. This explain the high conversion found at temperature of 653 K when using steam. The reaction pathway in the presence of steam also provides a smaller loss of selectivity by the unwanted deep oxidation, since a low concentration of C_4H_7 intermediate is expected to remain on the surface. If the temperature is increased to 900 K, water chemisorption can not any more stabilize the O surface species, and the measured influence of steam becomes insignificant.

Therefore the newly proposed mechanism reveals a major role of steam in 1-butene ODH reaction on Zn ferrite catalysts. Water stabilizes the active O site, even if it slightly reduces its reactivity for C-H bond activation. This influence of steam in 1-butene ODH reaction has not been observed experimentally or predicted theoretically so far to our knowledge. O species in oxide are important active sites for ODH reactions, which can be unstable by reduction at the high temperature at which the reaction is performed. The results obtained here could be generalized to propose an important role of water in stabilizing the surface O species in the form of highly stable hydroxyl species. Hence, we assume that our results will help to

understand the role of steam and hydroxylation in similar ODH reactions.

AUTHOR INFORMATION

Corresponding Authors
*yangwm.sshy@sinopec.com
*sautet@ucla.edu
ORCID
Tieqiang Zeng: 0000-0003-2073-3941
Philippe Sautet: 0000-0002-8444-3348

Notes

The authors declare no competing financial interest.

Supporting Information

Experimental characterization, additional energy diagrams and structure optimizations.

ACKNOWLEDGMENTS

The experiments were performed at Shanghai Research Institute of Petrochemical Technology. The DFT calculations were performed on the HOFFMAN2 cluster at the UCLA Institute for Digital Research and Education (IDRE).

REFERENCES

(1) Kuhlenbeck, H.; Shaikhutdinov, S.; Freund, H.-J. Well-Ordered Transition Metal Oxide Layers in Model Catalysis - A Series of Case Studies. Chem. Rev. **2013**, 113 (6), 3986-4034.
(2) Ketteler, G.; Weiss, W.; Ranke, W.; Schlögl, R. Bulk and surface phases of iron oxides in an oxygen and water atmosphere at low pressure. Phys. Chem. Chem. Phys. **2001**, 3 (6), 1114-1122.
(3) Schöttner, L.; Nefedov, A.; Yang, C.; Heissler, S.; Wang, Y.; Wöll, C. Structural evolution of α-Fe_2O_3(0001) surfaces under reduction conditions monitored by infrared spectroscopy. Front. Chem. **2019**, 7, 451.
(4) Rennard, R. J.; Kehl, W. L. Oxidative dehydrogenation of butenes over ferrite catalysts. J. Catal. **1971**, 21 (3), 282–293.
(5) Cares, W. R.; Hightower, J. W.; Ferrite spinels as catalysts in the oxidative dehydrogenation of butenes. J. Catal. **1971**, 23 (2), 193–203.
(6) Toledo-Antonio, J. A.; Nava, N.; Martínez, M.; Bokhimi, X. Correlation between the magnetism of non-stoichiometric zinc ferrites and their catalytic activity for oxidative dehydrogenation of 1-butene. Appl. Catal. A: Gen. **2002**, 234 (1-2), 137–144.
(7) Zhang, M.; Lan, R.; Liu, J.; Chen, X.; Zhou, W. Phase Cooperation between the $ZnFe_2O_4$ and α-Fe_2O_3 Phases of Ferrite Catalysts in the Oxidative Dehydrogenation of *n*-Butenes. J. Chem. Soc. Faraday Trans. **1992**, 88 (4), 637–644.
(8) Xu, W.-Q.; Yin, Y.-G.; Li, G.-Y.; Chen, S. Roles of spinel and maghemite phases in the oxidative dehydrogenation of butene over iron complex oxides II. Epitaxy and synergy between γ-Fe_2O_3 and ferrite spinels. Appl. Catal. A: Gen. **1992**, 89 (2), 131–142.
(9) Yang, B.; Liu, L.; Zou, G.; Luo, X.; Zhu, H.; Xu, S. The roles of $ZnFe_2O_4$ and α-Fe_2O_3 in the biphasic catalyst for the oxidative dehydrogenation of *n*-butene. J. Catal. **2020**, 381, 70–77.

(10) Batist, Ph. A.; Lippens, B. C.; Schuit, G. C. A. The Catalytic Oxidation of 1-Butene over Bismuth Molybdate Catalysts II. Dependence of Activity and Selectivity on the Catalyst Composition. J. Catal. **1966**, 5 (1), 55–64.
(11) Jung, J. C.; Kim, H.; Kim, Y. S.; Chung, Y.-M.; Kim, T. J.; Lee, S. J.; Oh, S.-H.; Song, I. K. Catalytic performance of bismuth molybdate catalysts in the oxidative dehydrogenation of C_4 raffinate-3 to 1,3-butadiene. Appl. Catal. A: Gen. **2007**, 317 (2), 244–249.
(12) Wan, C.; Cheng, D.-g.; Chen, F.; Zhan, X. The role of active phase in Ce modified BiMo catalysts for oxidative dehydrogenation of 1-butene. Catal. Today **2016**, 264, 180–184.
(13) López Nieto, J. M.; Concepción, P.; Dejoz, A.; Melo, F.; Knözinger, H.; Vázquez, M. I. Oxidative dehydrogenation of *n*-butane and 1-butene on undoped and K-doped VO_x/Al_2O_3 catalysts. Catal. Today **2000**, 61 (1-4), 361–367.
(14) López Nieto, J. M.; Concepción, P.; Dejoz, A.; Knözinger, H.; Melo, F.; Vázquez, M. I. Selective Oxidation of *n*-Butane and Butenes over Vanadium-Containing Catalysts. J. Catal. **2000**, 189 (1), 147–157.
(15) Furukawa, S.; Endo, M.; Komatsu, T. Bifunctional Catalytic System Effective for Oxidative Dehydrogenation of 1-Butene and *n*-Butane Using Pd-Based Intermetallic Compounds. ACS Catal. **2014**, 4 (10), 3533–3542.
(16) Yan, W.; Kouk, Q.-Y.; Tan, S. X.; Luo, J.; Liu, Y. Effects of Pt^0-PtO_x particle size on 1-butene oxidative dehydrogenation to 1,3-butadiene using CO_2 as soft oxidant. J. CO_2 Util. **2016**, 15, 154–159.
(17) Liu, X.; Su, D. S.; Schlögl, R. Oxidative dehydrogenation of 1-butene to butadiene over carbon nanotube catalysts. Carbon **2008**, 46 (3), 547–549.
(18) Massoth, F. E.; Scarpiello, D. A. Catalyst Characterization Studies on the Zn-Cr-Fe Oxide System. J. Catal. **1971**, 21 (3), 294–302.
(19) Li, X.; Cheng, D.-g.; Zhao, Z.-J.; Chen, F.; Gong, J. Temperature-induced deactivation mechanism of $ZnFe_2O_4$ for oxidative dehydrogenation of 1-butene. React. Chem. Eng. **2017**, 2 (2), 215–225.
(20) Li, X.; Paier, J. Adsorption of Water on the Fe_3O_4(111) Surface: Structures, Stabilities, and Vibrational Properties Studied by Density Functional Theory. J. Phys. Chem. C **2016**, 120, (2), 1056–1065.
(21) De Vrieze, J. E.; Thybaut, J. W.; Saeys, M. Role of Surface Hydroxyl Species in Copper-Catalyzed Hydrogenation of Ketones. ACS Catal. **2018**, 8 (8), 7539–7548.
(22) Köck, E.-M.; Kogler, M.; Klötzer, B.; Noisternig, M. F.; Penner, S. Structural and Electrochemical Properties of Physisorbed and Chemisorbed Water Layers on the Ceramic Oxides Y_2O_3, YSZ, and ZrO_2. ACS Appl. Mater. Interfaces **2016**, 8 (25), 16428–16443.
(23) Cao, S.; Liu, T.; Tsang, Y.; Chen, C. Role of hydroxylation modification on the structure and property of reduced graphene oxide/TiO_2 hybrids. Appl. Surf. Sci. **2016**, 382, 225–238.
(24) Li, S.-C.; Jacobson, P.; Zhao, S.-L.; Gong, X.-Q.; Diebold, U. Trapping Nitric Oxide by Surface Hydroxyls on Rutile TiO_2(110). J. Phys. Chem. C **2012**, 116 (2), 1887–1891.
(25) Chizallet, C.; Costentin, G.; Che, M.; Delbecq, F.; Sautet, P. Infrared Characterization of Hydroxyl Groups on MgO: A Periodic and Cluster Density Functional Theory Study. J. Am. Chem. Soc. **2007**, 129 (20), 6442−6452.
(26) Yan, G.; Wahler, T.; Schuster, R.; Schwarz, M.; Hohner, C.; Werner, K.; Libuda, J.; Sautet, P. Water on Oxide Surfaces: A Triaqua Surface Coordination Complex on Co_3O_4(111). J. Am.

Chem. Soc. **2019**, 141 (14), 5623−5627.
(27) Zhao, Z.-J.; Wu, T.; Xiong, C.; Sun, G.; Mu, R.; Zeng, L.; Gong, J. Hydroxyl-Mediated Non-oxidative Propane Dehydrogenation over VO_x/γ-Al_2O_3 Catalysts with Improved Stability. Angew. Chem. Int. Ed. **2018**, 57 (23), 6791−6795.
(28) Gu, Q.; Sautet, P.; Michel, C. Unraveling the Role of Base and Catalyst Polarization in Alcohol Oxidation on Au and Pt in Water. ACS Catal. **2014**, 4 (11), 4004-4014.
(29) Wang, M.; Ai, Z.; Zhang, L. Generalized Preparation of Porous Nanocrystalline $ZnFe_2O_4$ Superstructures from Zinc Ferrioxalate Precursor and Its Superparamagnetic Property. J. Phys. Chem. C **2008**, 112 (34), 13163–13170.
(30) Tabari, T.; Singh, D.; Jamali, S. S. Enhanced photocatalytic activity of mesoporous $ZnFe_2O_4$ nanoparticles towards gaseous benzene under visible light irradiation. J. Environ. Chem. Eng. **2017**, 5 (1), 931–939.
(31) Yang, B. L.; Cheng, D. S.; Lee, S. B. Effect of steam on the oxidative dehydrogenation of butene over magnesium ferrites with and without chromium substitution. Appl. Catal. **1991**, 70 (2), 161–173.
(32) Li, G.; Zhu, X.; Song, W.; Yang, Z.; Dai, J.; Sun, Y.; Fu, Y. Annealing effects on semitransparent and ferromagnetic $ZnFe_2O_4$ nanostructured films by sol-gel. J. Am. Ceram. Soc. **2011**, 94 (9), 2872–2877.
(33) Kresse, G.; Hafner, J. Ab Initio Molecular Dynamics for Liquid Metals, Phys. Rev. B **1993**, 47 (1), 558–561.
(34) Kresse, G.; Furthmüller, J., Efficiency of Ab-Initio Total Energy Calculations for Metals and Semiconductors Using a Plane-Wave Basis Set. Comput. Mater. Sci. **1996**, 6 (1), 15–50.
(35) Blöchl, P. E. Projector augmented-wave method. Phys. Rev. B **1994**, 50 (24), 17953−17979.
(36) Kresse, G.; Joubert, D. From ultrasoft pseudopotentials to the projector augmented-wave method. Phys. Rev. B **1999**, 59 (3), 1758−1775.
(37) Perdew, J. P.; Burke, K.; Ernzerhof, M., Generalized Gradient Approximation Made Simple. Phys. Rev. Lett. **1996**, 77 (18), 3865–3868.
(38) Steinmann, S. N.; Corminboeuf, C. Comprehensive Benchmarking of a Density-Dependent Dispersion Correction. J. Chem. Theory Comput. **2011**, 7 (11), 3567–3577.
(39) Guo, H.; Marschilok, A. C.; Takeuchi, K. J.; Takeuchi, E. S.; Liu, P. Essential Role of Spinel $ZnFe_2O_4$ Surfaces during Lithiation. ACS Appl. Mater. Interfaces **2018**, 10 (41), 35623−35630.
(40) Zhang, Y.; Pelliccione, C. J.; Brady, A. B.; Guo, H.; Smith, P. F.; Liu, P.; Marschilok, A. C.; Takeuchi, K. J.; Takeuchi, E. S. Probing the Li Insertion Mechanism of $ZnFe_2O_4$ in Li-Ion Batteries: A Combined X-Ray Diffraction, Extended X-Ray Absorption Fine Structure, and Density Functional Theory Study. Chem. Mater. **2017**, 29 (10), 4282−4292.
(41) Yu, X.; Li, Y.; Li, Y.-W.; Wang, J.; Jiao, H. DFT+U Study of Molecular and Dissociative Water Adsorptions on the Fe_3O_4 (110) Surface. J. Phys. Chem. C **2013**, 117 (15), 7648−7655.
(42) Hill, T. L. An Introduction to Statistical Thermodynamics; Addison Wesley Publishing Company: Reading, MA, 1960; pp 161−176.
(43) Henkelman, G.; Uberuaga, B. P.; Jónsson, H. A climbing image nudged elastic band method for finding saddle points and minimum energy paths. J. Chem. Phys. **2000**, 113 (22), 9901−9904.

(44) Henkelman, G.; Jónsson, H. Improved tangent estimate in the nudged elastic band method for finding minimum energy paths and saddle points. J. Chem. Phys. **2000**, 113 (22), 9978−9985.
(45) Kamazawa, K.; Tsunoda, Y.; Kadowaki, H.; Kohn, K. Magnetic neutron scattering measurements on a single crystal of frustrated $ZnFe_2O_4$. Phys. Rev. B **2003**, 68 (2), 024412/1−024412/9.
(46) Schiessl, W.; Potzel, W.; Karzel, H.; Steiner, M.; Kalvius, G. M.; Martin, A.; Krause, M. K.; Halevy, I.; Gal, J.; Schäfer, W.; Will, G.; Hillberg, M.; Wäppling, R. Magnetic Properties of the $ZnFe_2O_4$ Spinel. Phys. Rev. B **1996**, 53 (14), 9143−9152.
(47) Melo Quintero, J. J.; Rodríguez Torres, C. E.; Errico, L. A. Ab initio calculation of structural, electronic and magnetic properties and hyperfine parameters at the Fe sites of pristine $ZnFe_2O_4$. J. Alloys Compd. **2018**, 741, 746−755.
(48) Melo Quintero, J. J.; Salcedo Rodríguez, K. L.; Rodríguez Torres, C. E.; Errico, L. A. Ab initio study of the role of defects on the magnetic response and the structural, electronic and hyperfine properties of $ZnFe_2O_4$. J. Alloys Compd. **2019**, 775, 1117−1128.
(49) Rishikeshi, S. N.; Joshi, S. S.; Temgire, M. K.; Bellare, J. R. Chain length dependence of polyol synthesis of zinc ferrite nanoparticles: why is diethylene glycol so different? Dalton Trans. **2013**, 42 (15), 5430−5438.
(50) Salcedo Rodríguez, K. L.; Hoffmann, M.; Golmar, F.; Pasquevich, G.; Werner, P.; Hergert, W.; Rodríguez Torres, C. E. Producing $ZnFe_2O_4$ thin films from ZnO/FeO multilayers. Appl. Surf. Sci. **2017**, 393, 256–261.
(51) Yamashita, T.; Hayes, P. Analysis of XPS spectra of Fe^{2+} and Fe^{3+} ions in oxide materials. Appl. Surf. Sci. **2008**, 254 (8), 2441−2449.
(52) Briggs, D.; Seah, M.P. Practical Surface Analysis by Auger and X-ray Photoelectron Spectroscopy; John Wiley & Sons: New York, 1990; pp 143-144.
(53) Li, X.; Paier, J.; Sauer, J.; Mirabella, F.; Zaki, E.; Ivars-Barceló, F.; Shaikhutdinov, S.; Freund, H.-J. Surface Termination of Fe_3O_4(111) Films Studied by CO Adsorption Revisited. J. Phys. Chem. B **2018**, 122 (2), 527−533.
(54) Huang, D.-M.; Cao, D.-B.; Li, Y.-W.; Jiao H. Density Function Theory Study of CO Adsorption on Fe_3O_4(111) Surface. J. Phys. Chem. B **2006**, 110 (28), 13920−13925.
(55) Kung, H. H.; Kung, M. C. Selective oxidative dehydrogenation of butenes on ferrite catalysts. Adv. Catal. **1985**, 33, 159−198.
(56) Redhead, P. A. Thermal desorption of gases. Vacuum **1962**, 12, 203−211.
(57) Misono, M.; Sakata, K.; Ueda, F.; Nozawa, Y.; Yoneda, Y. Catalytic Properties of Iron Oxide. III. Oxidative Dehydrogenation of Butenes over Iron Oxide Catalysts. Bull. Chem. Soc. Jpn. **1980**, 53 (3), 648−652.
(58) Kozuch, S.; Shaik, S. How to Conceptualize Catalytic Cycles? The Energetic Span Model. Acc. Chem. Res. **2011**, 44 (2), 101–110.

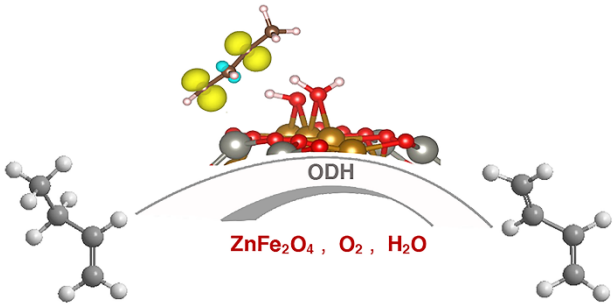
ODH
ZnFe2O4 , O2 , H2O